Langmuir
Article
pubs.acs.org/Langmuir


# Local Velocity Measurements in the Shear-Thickening Transition of Dilute Micellar Solutions of Surfactants

Jalal Dehmoune

*Laboratory of the Future, CNRS, Université Bordeaux I, Rhodia, 178 avenue du Dr Schweitzer, 33608 Pessac cedex, France*

Sébastien Manneville

*Laboratoire de Physique, École Normale Supérieure de Lyon 46 allée d'Italie, 69364 Lyon cedex 07, France*

Jean-Paul Decruppe*

*Laboratoire de Physique des Milieux Denses, Université Paul Verlaine, 1 boulevard Arago, 57078 Metz cedex 3, France*

*Received September 14, 2010. Revised Manuscript Received November 15, 2010*

Local velocimetry and rheometric measurements are performed on three dilute micellar solutions which undergo the shear-thickening transition. The three surfactants, namely, alkyltrimethyl ammonium bromide ($C_n$TAB), all belong to the same family and only differ by the length of the aliphatic chain. Simultaneous ultrasonic velocimetry and rheometry recordings provide convincing evidence for a heterogeneous flow in the shear-thickening domain. A detailed analysis allows us to demonstrate surprisingly similar evolutions of the wall slip magnitude and of the apparent viscosity as well as subtle differences between the three systems. Together with the velocimetry results, the direct observation of the flow in the vorticity−velocity plane reveals that the shear-thickening transition is associated with the emergence of a three-dimensional unstable flow.

## I. Introduction

It is well-known that surfactants self-assemble to form various supramolecular structures in solutions. Spherical[1] and cylindrical micelles[2] are commonly observed in surfactant solutions and are among the simplest shapes that one can observe in the dilute or semidilute concentration domains. The flow behavior of dilute aqueous micellar solutions presents a rich and often unexpected behavior. A good example is the shear-thickening transition, that is, the increase of the apparent viscosity at a critical shar rate $\dot{\gamma}_c$ or critical shear stress $\sigma_c$.[3−9] The amplitude and shape of the shear-thickening depend on various parameters such as the surfactant chemical characteristics, the nature of the counterion, and their concentrations. Most previous studies agree on the conclusion that shear-thickening is due to the formation of a "shear induced structure" (SIS). Common characteristics of the shear-thickening transition and of the SIS are as follows:

(I) The transition occurs in surfactant solutions in which spherical or cylindrical micelles are known to exist at equilibrium.[7,8,10]

(II) The transition happens in a system having a low-shear viscosity very close to the solvent viscosity (pure water, most of the time[5,7]).

(III) The emergence of the SIS induces a sharp increase of the birefringence intensity and a decrease of the extinction angle $\chi$ to a value close to zero.[5]

(IV) At the transition, small angle neutron scattering (SANS) patterns lose their circular symmetry to take the shape of elongated ellipsoids when the viscosity starts to increase.[11,10]

(V) It has also been shown that the SIS has properties similar to a gel.[8,13,12]

According to previous direct visualizations[8] and SANS experiments,[14] during shear-thickening, there is evidence for the coexistence of two mixed phases: the SIS and a fluid phase (FP). However, the fundamental mechanism of the SIS formation which is responsible for the sudden increase of the viscosity is still the subject of debate,[3−8] and various models have been proposed where the SIS corresponds to supramolecular aggregates resulting from a fusion mechanism of the micelles,[7,8,15] to microscopic aggregates of a sponge phase,[16] to a necklace of oriented micelle rings,[17] or to bundles of aggregated micelles.[18]

*To whom correspondence should be addressed. E-mail: decruppe@univ-metz.fr.

(1) Kalus, J.; Hofmann, H.; Reizlein, K.; Ulbricht, W.; Ibel, K. *Ber. Bunsen-Ges.* **1982**, *86*, 31.
(2) Bendedouch, D.; Chen, S. H.; Koehler, W. C. *J. Phys. Chem.* **1983**, *87*, 153.
(3) Gamez-Corrales, R.; Berret, J. F.; Walker, L. M.; Oberdisse, J. *Langmuir* **1999**, *15*, 6755.
(4) Hu, Y.; Rajaram, C. V.; Wang, S. Q.; Jamieson, A. M. *Langmuir* **1994**, *10*, 80.
(5) Dehmoune, J.; Decruppe, J. P.; Greffier, O.; Xu, H. *Rheol. Acta* **2007**, *46*, 1121.
(6) Dehmoune, J.; Decruppe, J. P.; Greffier, O.; Xu, H. *J. Rheol.* **2008**, *52*, 923.
(7) Rehage, H.; Hoffmann, H. *Rheol. Acta* **1982**, *21*, 561.
(8) Liu, C. H.; Pine, D. J. *Phys. Rev. Lett.* **1996**, *77*, 2121.
(9) Berret, J. F.; Lerouge, S. *arXiv.org*, [cond-mat.soft] **2009**, *0910*, 1854.
(10) Dehmoune, J.; Decruppe, J. P.; Greffier, O.; Xu, H. *Langmuir* **2009**, *25*, 7271.
(11) Berret, J. F.; Gamez-Corrales, R.; Serero, Y.; Molino, F.; Lindner, P. *Europhys. Lett.* **2001**, *54*, 605.
(12) Rehage, H.; Hoffmann, H.; Wunderlich, I. *Ber. Bunsen-Ges.* **1986**, *90*, 1071.
(13) Wunderlich, I.; Hoffmann, H.; Rehage, H. *Rheol. Acta* **1987**, *26*, 532.
(14) Kalus, J.; Hoffmann, H.; Chen, S. H.; Linder, P. *J. Phys. Chem.* **1989**, *93*, 4267.
(15) Boltenhagen, P.; Yu, H.; Matthys, E. F.; Pine, D. J. *Europhys. Lett.* **1997**, *38*, 389.
(16) Hoffmann, H.; Hoffmann, S.; Rausher, A.; Kalus, J. *Prog. J. Colloid Polym. Sci.* **1991**, *84*, 24.
(17) Hoffmann, S.; Rauscher, A.; Hoffmann, H. *Ber. Bunsen-Ges.* **1991**, *95*, 153.
(18) Barentin, C.; Liu, A. J. *Europhys. Lett.* **2001**, *55*, 432.

Complementary experimental studies thus seem necessary in order to obtain new information about the characteristics of the shear-thickening transition in dilute surfactant solutions. Recently, we reported rheometric, rheo-optical, and SANS results experiments performed on three surfactant−salt systems $C_nTAB$/NaSal/$H_2O$, with $n$ = 14, 16, and 18, only differing by the length of the aliphatic chain, at the low concentration of 3 mM/3 mM.[5,6,10] These dilute systems were shown to follow a complex rheological behavior with successive Newtonian or shear-thinning, shear-thickening, and shear-thinning behaviors as the shear rate is increased. The aim of the present paper is to measure and compare the local flow behaviors of these three micellar systems. To do so, we shall perform rheological characterizations, ultrasonic velocimetry experiments in the velocity-shear rate plane, and finally direct visualization in the vorticity−velocity plane. By coupling those three measurement techniques, we hope to shed new light on the role played by the SIS on the flow field in the shear-thickening domain.

## II. Materials and Methods

**A. Samples.** In order to obtain the highest shear-thickening magnitude, it was shown that the following conditions should be met:

(I) The concentration of the sample has to be chosen so that the sample remains in the dilute regime or in the vicinity of the semidilute regime close to the overlap concentration $C^*$.[4,7−9,17]

(II) The best counterion to be used with $C_nTAB$ surfactants is the salicylate ion, $Sal^-$.[19]

(III) The salt should be added at a concentration leading to an equimolar solution.[4]

The surfactants used in the present work are octadecyl trimethyl ammonium bromide $C_{18}TAB$ (Aldrich), cetyl trimethyl ammonium bromide $C_{16}TAB$ (Aldrich), and myristyl trimethyl ammonium bromide $C_{14}TAB$ (Acros). The systems under study are ternary mixtures of $C_nTAB$, sodium salycilate NaSal (Aldrich), and water. The salt plays the role of a counterion which reduces the electrostatic repulsion between the polar heads, thus favoring the growth of the micelles. The required amounts of surfactant and salt are carefully weighted with a precision of $\pm 10^{-5}$ g and mixed with filtered water at a temperature of 23 ± 0.1 °C. The samples are sonicated for a few hours and then left at rest to reach equilibrium at 32 ± 0.2 °C for at least 3 days prior to any experiments.

Here we focus on $C_nTAB$/NaSal systems at 3 mM/3 mM because the micellar shapes at rest differ for $n$ = 14, 16, and 18: $C_{18}TAB$ and $C_{16}TAB$ micelles are cylindrical and already entangled at 3 mM, while at the same concentration $C_{14}TAB$ only gives slightly asymmetrical micelles.[10]

**B. Rheometry Devices and Protocol.** For the rheometric measurements, two rheometers were used: a stress-imposed AR-1000 rheometer (TA Instruments) and a strain-controlled RFS III rheometer (TA Instruments). The velocimetry measurements are performed simultaneously to the rheometric characterizations in a Couette cell as described below. In all the experiments, the temperature is kept constant at 23 ± 0.1 °C.

The experimental procedure is similar to the one described in our previous studies.[5,6,10] The sample is subjected to a shear rate $\dot{\gamma}$ which is gradually increased with six different values of $\dot{\gamma}$ per decade. Each shear rate is applied during 600 s prior to any measurement of the corresponding shear stress value. We checked that this duration is long enough for the shear stress to reach a steady state.[6]

The apparent macroscopic viscosity $\eta$ is then simply calculated as the ratio $\eta = \sigma/\dot{\gamma}$ of the measured shear stress $\sigma$ to the applied shear rate $\dot{\gamma}$, which will also be noted $\dot{\gamma}_M$ below to clearly distinguish this macroscopic shear rate from a local shear rate whenever necessary.

**C. High Frequency Ultrasonic Speckle Velocimetry (USV).** The sample velocity field is measured using ultrasonic speckle velocimetry (USV) at about 15 mm from the cell bottom. USV is a technique that allows one to access velocity profiles in Couette geometry with a spatial resolution of 40 $\mu$m and a temporal resolution that depends on the applied shear rate. Full details about USV may be found in ref 20. Here, we only recall those features of USV that are relevant to the present study.

USV relies on the analysis of ultrasonic speckle signals that result from the interferences of the backscattered echoes of successive incident pulses of central frequency 36 MHz generated by a high-frequency piezo-polymer transducer (Panametrics PI50-2) connected to a broadband pulser-receiver (Panametrics 5900PR with 200 MHz bandwidth). The speckle signals are sent to a high-speed digitizer (Acqiris DP235 with 500 MHz sampling frequency) and stored on a PC for postprocessing using a cross-correlation algorithm that yields the local displacement from one pulse to another as a function of the radial position across the gap. After a calibration step using a Newtonian fluid (see ref 20), tangential velocity profiles are then obtained by averaging over typically 1000 successive cross-correlations.

USV has already been successfully used on different micellar systems.[21−24] Since such systems are transparent to ultrasound, a small amount of polystyrene particles (1 wt %) with an average diameter of 5 $\mu$m is added to the samples in order to provide some acoustic contrast. The time needed to record a single velocity profile varies from 0.1 s at the highest shear rates of about 400 $s^{-1}$ to 40 s at the lowest shear rates of about 1 $s^{-1}$. Simultaneous rheological experiments and USV measurements are conducted in the gap of a Plexiglas Couette device of gap width $e$ = 0.95 mm and outer radius $R_2$ = 25 mm. In the following, for each applied shear rate, we shall focus on velocity profiles averaged over 20 successive measurements recorded once the shear stress has reached steady state. Error bars are then calculated from the standard deviation of those 20 measurements and, in the case of an unsteady flow, give an estimate of the temporal fluctuations of the velocity within the sample.

Finally, it should be noted that USV actually measures the projection of the velocity vector along the acoustic axis which makes some angle $\theta \simeq 15°$ with the radial direction, so that the general expression of the USV velocity measurement reads:[23]

$$V(r) = V_\theta(r) + \frac{V_r(r)}{\tan\theta} \quad (1)$$

where $r$ is the radial distance to the rotation axis and $V_\theta$ and $V_r$, respectively, denote the tangential and radial components of the velocity vector. Therefore, when the flow is purely tangential, the USV measurement yields the tangential velocity profile. However, the interpretation of the experimental velocity profiles $V(r)$ may become problematic whenever the flow is not purely tangential, since in this case the USV measurements contain contributions from both $V_\theta$ and $V_r$. Moreover, since $\tan\theta \simeq 0.25$, the effect of the radial velocity is amplified by a factor of about 4 due to the second term in eq 1.

## III. Rheological Properties of Pure and Seeded Solutions

The viscosity curve $\eta(\dot{\gamma})$ of shear-thickening micellar system appears to be constituted of three parts.[5,6] These regions will be

(19) Hartmann, V.; Cressely, R. *Colloids Surf.* **1997**, *121*, 151.

(20) Manneville, S.; Bécu, L.; Colin, A. *Eur. Phys. J.: Appl. Phys.* **2004**, *28*, 361.
(21) Bécu, L.; Manneville, S.; Colin, A. *Phys. Rev. Lett.* **2004**, *93*, 18301.
(22) Decruppe, J. P.; Greffier, O.; Manneville, S.; Lerouge, S. *Phys. Rev. E* **2006**, *73*, 061509.
(23) Bécu, L.; Anache, D.; Manneville, S.; Colin, A. *Phys. Rev. E* **2007**, *76*, 011503.
(24) Manneville, S.; Colin, A.; Waton, G.; Schosseler, F. *Phys. Rev. E* **2007**, *75*, 061502.

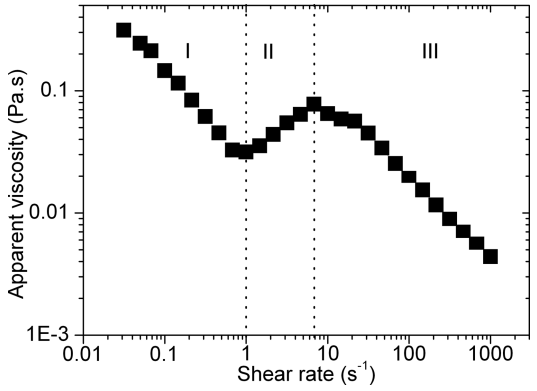


**Figure 1.** Apparent macroscopic viscosity $\eta$ versus the applied shear rate $\dot{\gamma}$ for $C_{18}$TAB (■). The vertical dashed lines indicate the boundaries of the three domains (see text).

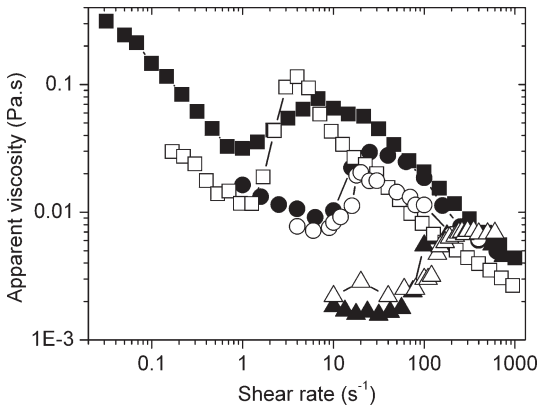


**Figure 2.** Apparent macroscopic viscosity versus the applied shear rate for the three surfactants $C_{18}$TAB (■/□), $C_{16}$TAB (●/○), and $C_{14}$TAB (▲/△). Full symbols refer to pure solutions, and empty symbols to solutions seeded with 1 wt % polystyrene spheres.

denoted domains I, II, and III according to the shear rate range that they cover (see Figure 1 where the boundaries between the three domains are shown for the $C_{18}$TAB solution). Domain I comes before the shear-thickening transition. Domain II corresponds to the increasing part of the viscosity curve: it starts at $\dot{\gamma}_c$ and ends when $\dot{\gamma} = \dot{\gamma}_m$ which is the abscissa of the viscosity maximum $\eta_m$. Finally, domain III is the remaining part extending after the maximum in the $\eta(\dot{\gamma})$ curve.

While the raw micellar solutions of $C_{18}$TAB, $C_{16}$TAB, and $C_{14}$TAB are optically transparent, the samples seeded with polystyrene particles are slightly turbid. Since the concentration of the particles (1 wt %) is of the same order of magnitude as the amount of surfactant and counterion at 3 mM, one may wonder whether the particles introduced into the samples affect the macroscopic behavior of the micellar systems. It is therefore essential to first study the effect of the particles on the rheological properties of the dilute solutions.

Figure 2 reports the variations of the apparent macroscopic viscosity as a function of the applied shear rate for solutions containing particles (empty symbols) and samples free of particles (full symbols). The curves are qualitatively the same for both cases so that polystyrene seeding particles at 1 wt % do not significantly affect the rheological behavior of $C_n$TAB/NaSal at 3 mM/3 mM. In particular, the critical shear rate $\dot{\gamma}_c$ remains unchanged when particles are added to the system. The only notable difference concerns the shear-thickening domain of $C_{18}$TAB for which a sharper and narrower viscosity peak is observed for the solution that contains seeding particles.

**Table 1. Fitted Values of the Parameters $n$ and $\kappa$ of the Ostwald−de Waele Model in the Three Domains of the Flow Curves for the Three Surfactants without Seeding Particles**

| | surfactant | | | | | |
|---|---|---|---|---|---|---|
| | $C_{14}$TAB | | $C_{16}$TAB | | $C_{18}$TAB | |
| domain | $n$ | $\kappa$ | $n$ | $\kappa$ | $n$ | $\kappa$ |
| I | 0.98 | 0.002 | 0.71 | 0.015 | 0.23 | 0.025 |
| II | 1.29 | 0.0013 | 1.25 | 0.011 | 1.5 | 0.030 |
| III | 0.40 | 0.234 | 0.30 | 0.41 | 0.33 | 0.42 |

In domain I, $C_{18}$TAB and $C_{16}$TAB are characterized by a shear-thinning behavior while $C_{14}$TAB presents a Newtonian plateau. The three systems then undergo the shear-thickening transition, which is characterized by an increase of the apparent viscosity by a factor of about 5, at widely different critical shear rates $\dot{\gamma}_c$. Indeed, the critical shear rate $\dot{\gamma}_c$ increases by 2 orders of magnitude when the chain length decreases from $C_{18}$TAB to $C_{14}$TAB while the viscosity only decreases by a factor 10, so that the energy ($\propto \eta\dot{\gamma}_c^2$) required to reach and trigger the shear-thickening transition is much higher in solutions of surfactants with a shorter chain length.

At the end of domain II, birefringence experiments show that the average orientation of the micelles is close to the flow direction.[6] For higher shear rates, the behavior of the three systems is surprisingly similar: within experimental error, all three curves superimpose; that is, the rheological behavior is the same for the three surfactants and thus becomes independent of the chain length.

Finally, to better quantify the above rheological behavior, the experimental data for the raw micellar solutions were fitted by an Ostwald−de Waele (power-law) model with two parameters:

$$\sigma = \kappa\dot{\gamma}^n \tag{2}$$

where $\kappa$ and $n$ are two constants and $n < 1$ and $n > 1$, respectively, correspond to shear-thinning and shear-thickening fluids. The best fit results are listed in Table 1 for each of the three domains of the flow curves. In domain I, the parameter $n$ varies from 0.98 for $C_{14}$TAB to 0.23 for $C_{18}$TAB. Compared to $C_{14}$TAB, the latter value reveals the strong non-Newtonian and viscoelastic behavior of $C_{18}$TAB even at this low surfactant concentration (3 mM).

## IV. Velocimetry Results in Couette Geometry

In this section, we investigate the flow behaviors of $C_{18}$TAB, $C_{16}$TAB, and $C_{14}$TAB by comparing velocity profiles measured using USV in the three domains. It should be kept in mind that when the flow is not purely tangential, the USV measurements may include a non-negligible contribution of the radial velocity according to eq 1. For clarity, we will only show the velocity profiles for some representative shear rates. In Figures 3−8 below, the experimental velocity $V(x)$ is drawn using ● or ■ symbols as a function of the normalized position $x = (r - R_1)/e$ in the gap, where $R_1$ is the radius of the moving inner wall and $e = R_2 - R_1$ is the gap width. The abscissae $x = 0$ and $x = 1$ thus, correspond, respectively to the positions of the rotor and the stator. The maximum value on the $y$-axis represents the value of the tangential velocity $V_M$ of the inner cylinder. The straight dashed line joining the upper left corner to the bottom right one shows the velocity profile expected in the case of a Newtonian fluid in the absence of wall slip.

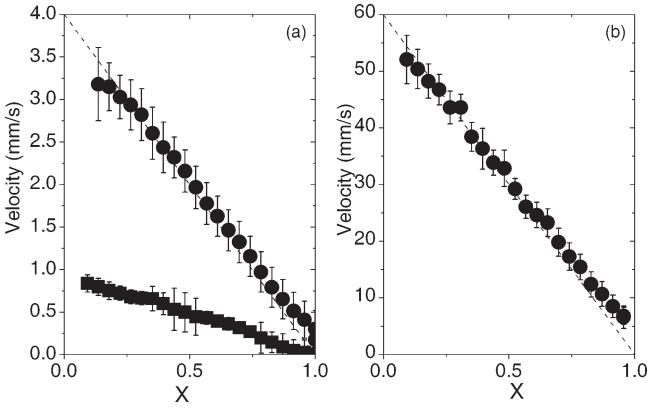


**Figure 3.** Velocity profiles $V(x)$ in domain I for (a) $C_{18}$TAB at 1 $s^{-1}$ (■) and $C_{16}$TAB at 4 $s^{-1}$ (●), and (b) $C_{14}$TAB at 60 $s^{-1}$.

The local shear rate $\dot{\gamma}(x)$ can be easily estimated by differentiating the velocity profile as a function of $x$. Once $\dot{\gamma}(x)$ is known, the distribution of the effective local viscosity $\eta_e(x)$ is also simply computed across the gap by dividing the macroscopic shear stress (measured by the shearing device) by the local shear rate $\dot{\gamma}(x)$: $\eta_e(x) = \sigma(x)/\dot{\gamma}(x) \simeq \sigma/\dot{\gamma}(x)$, where $\sigma$ is the macroscopic stress which, in small gap conditions, remains always close to the local stress $\sigma(x)$. In the following, due to the large noise introduced by the differentiation of experimental velocity profiles, we shall only focus on spatially averaged values of $\dot{\gamma}(x)$ and $\eta_e(x)$, that will be denoted $\overline{\dot{\gamma}}$ and $\overline{\eta}$, respectively, taken over various portions of the velocity profile depending on its shape.

**A. Velocity Profiles at Low Macroscopic Shear Rates (Domain I).** The velocity profiles of $C_{18}$TAB, $C_{16}$TAB, and $C_{14}$TAB are shown in Figure 3 for a single value of the shear rate in domain I, respectively, 1, 4, and 60 $s^{-1}$. For the three surfactants, the velocity profile is close to a Newtonian distribution, but a small amount of wall slip (about 10% of the inner wall velocity) is observed for $C_{16}$TAB and $C_{14}$TAB. The large error bars observed for $C_{18}$TAB can be attributed to the fast sedimentation of the seeding particles, which leads to a lack of ultrasonic speckle signal at such a low shear rate and thus to a large uncertainty at some points in the gap. The size of the error bars for the two other samples is typical of the USV measurement uncertainty for a stationary flow.

Although rheological experiments have shown that $C_{18}$TAB and $C_{16}$TAB behave like shear-thinning fluids prior to the shear-thickening transition (see Table 1), this non-Newtonian behavior does not clearly appear in the velocity profiles which all remain very close to linear. This is easily explained by considering the theoretical expression of the velocity profile for a fluid following the Ostwald–de Waele equation (see eq 2) with no-slip boundary conditions at the walls (i.e., $V = 0$ for $r = R_2$ and $V = V_M$ for $r = R_1$):[25]

$$V(r) = Cr\left[\left(\frac{R_2}{r}\right)^{2/n} - 1\right] \quad (3)$$

where

$$C = \frac{V_M {R_1}^{2/n-1}}{{R_2}^{2/n} - {R_1}^{2/n}}$$

(25) Salmon, J. B.; Manneville, S.; Colin, A.; Molino, F. *Phys. Rev. Lett.* **2003**, *90*, 228303.

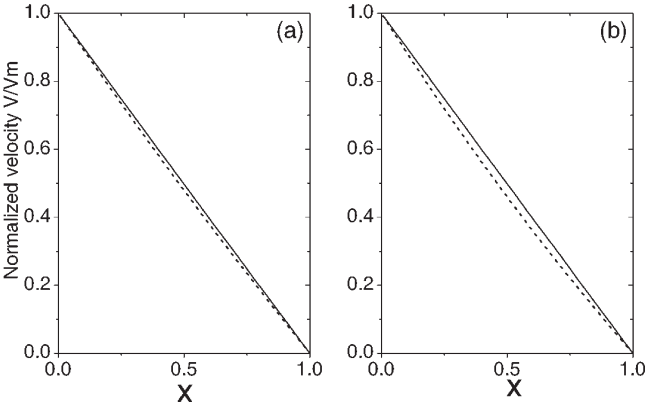


**Figure 4.** Normalized velocity profiles $V(x)/V_M$ (short dash) computed from eq 4 for (a) $C_{14}$TAB with $n = 0.98$ and (b) $C_{18}$TAB with $n = 0.23$. The velocity profiles are both very close to linear (full line).

**Table 2. Average Viscosity $\overline{\eta}$ Deduced from the Local Viscosity $\eta_e(x)$ Compared to the Macroscopic Viscosity $\eta$ for the Three Surfactants in Domain I**

| | viscosity | |
|---|---|---|
| | $\overline{\eta}$ (mPa·s) | $\eta$ (mPa·s) |
| $C_{18}$TAB | 38 | 31 |
| $C_{16}$TAB | 12 | 10 |
| $C_{14}$TAB | 23 | 21 |

Using the normalized position $x \in [0,1]$, one gets

$$V(x) = CR_1\left(1 + \frac{e}{R_1}x\right)\left[\left(\frac{R_2}{R_1}\right)^{2/n}\left(1 + \frac{e}{R1}x\right)^{-2/n} - 1\right] \quad (4)$$

In our experiments, the "small-gap approximation" $e/R_1 \ll 1$ holds since $e/R_1 \simeq 0.04$. In this case, one has $C \simeq nV_M/(2e)$ and a first order expansion of eq 4 yields simply $V(x) = V_M(1 - x)$. Such a linear velocity profile in the small-gap approximation, independent of the value of $n$, explains why the experimental profiles cannot be distinguished from Newtonian profiles in spite of pronounced shear-thinning. This is also confirmed by Figure 4 which shows a few theoretical velocity profiles computed using eq 4 and some of the values of the exponent $n$ shown in Table 1 while neglecting apparent wall slip at the cell boundaries. The largest deviation from linearity is observed in Figure 4b for $C_{18}$TAB in domain I ($n = 0.23$), but even so the uncertainty on the USV velocity measurements does not allow us to distinguish between shear-thinning and Newtonian behaviours.

Finally, the viscosity $\overline{\eta}$ computed by averaging $\eta_e(x)$ over the whole gap is shown in Table 2. $\overline{\eta}$ is found to be systematically larger than the macroscopic viscosity measured by the rheometer, which is due to the presence of small but noticeable wall slip.

**B. Velocity Profiles in the Shear-Thickening Domain (Domain II).** Figures 5–7 present the velocity profiles $V(x)$ for several shear rates chosen in the shear-thickening domain of the three surfactants. In most cases, an overall qualitative examination of the profiles shows that they can be clearly divided into two segments (labeled A and B) corresponding to fluid layers with different flow behaviors. Tables 3–5 show the average effective shear rate $\dot{\gamma}$ and viscosity $\overline{\eta}$ estimated in each segment, together with the macroscopic applied shear rate $\dot{\gamma}_M$ and apparent viscosity $\eta$ recorded by the rheometer. The distribution of the effective viscosity and its variations will provide an indicator of the distribution of the SIS across the gap.

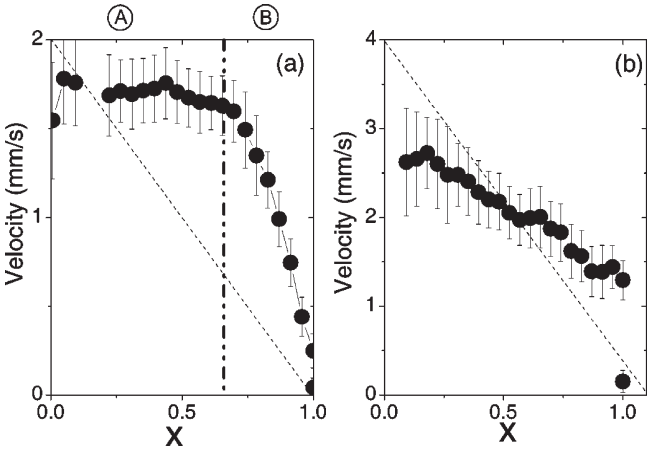


**Figure 5.** $C_{18}TAB$ in the shear-thickening domain. Velocity profiles $V(x)$ in domain II for (a) $\dot{\gamma}_M = 2\ s^{-1}$ and (b) $4\ s^{-1}$.

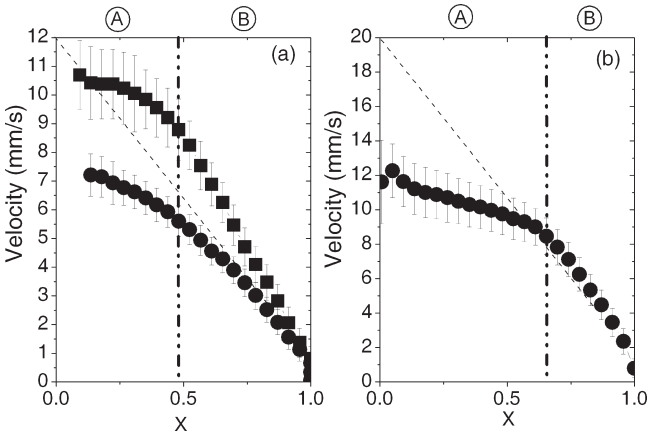


**Figure 6.** $C_{16}TAB$ in the shear-thickening domain. Velocity profiles $V(x)$ in domain II for (a) $\dot{\gamma}_M = 8\ s^{-1}$ (●) and $12\ s^{-1}$ (■), and (b) $\dot{\gamma}_M = 20\ s^{-1}$.

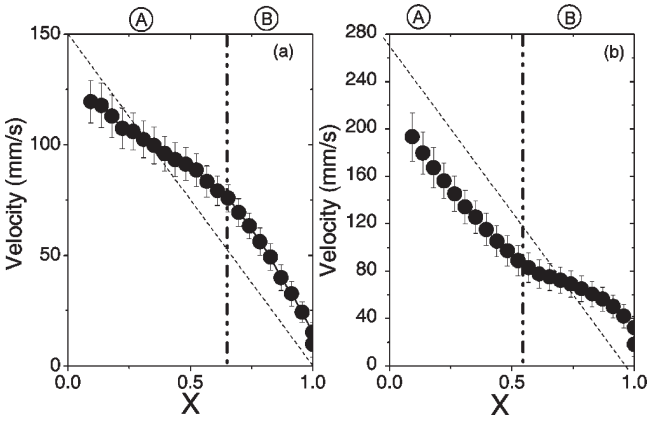


**Figure 7.** $C_{14}TAB$ in the shear-thickening domain. Velocity profiles $V(x)$ in domain II for (a) $\dot{\gamma}_M = 150\ s^{-1}$ and (b) $280\ s^{-1}$.

*1. $C_{18}TAB$ in the Shear-Thickening Domain (II).* The velocity profiles for $C_{18}TAB$ are shown in Figure 5 for $\dot{\gamma}_M = 2$ and $4\ s^{-1}$ which are, respectively, close to the critical shear rate $\dot{\gamma}_c$ triggering the shear-thickening transition and to $\dot{\gamma}_m$.

At $\dot{\gamma}_M = 2\ s^{-1}$, $V(x)$ can be divided into two segments A and B with very different slopes (see Figure 5a and Table 3). Close to the moving wall (segment A), the velocity profile decreases very slowly as a function of the position $x$, leading to a very small average local shear rate ($\bar{\dot{\gamma}} = 0.27\ s^{-1}$). In this almost flat part of the velocity profile, the average viscosity of the fluid is about 170 mPa·s, nearly 6 times the apparent viscosity $\eta \simeq 30$ mPa·s. This pluglike flow is consistent with the description of the SIS in terms of a highly viscous "gel" phase that rotates as a solid-body.[8,29] Wall slip at the inner wall remains of the same order as in domain I. Close to the fixed wall (segment B), $V(x)$ linearly decreases to

**Table 3. Macroscopic Shear Rate $\dot{\gamma}_M$ and Apparent Viscosity $\eta$ Compared to the Effective Average Shear Rate $\bar{\dot{\gamma}}$ and Viscosity $\bar{\eta}$ of $C_{18}TAB$ in the Different Segments at $\dot{\gamma}_M = 2\ s^{-1}$ (Domain II)**

| $\dot{\gamma}_M = 2\ (s^{-1})$ and $\eta = 31$ (mPa·s) | | |
|---|---|---|
| | average values | |
| | $\bar{\dot{\gamma}}\ (s^{-1})$ | $\bar{\eta}$ (mPa·s) |
| segment A | 0.27 | 170 |
| segment B | 4.5 | 7 |

**Table 4. Macroscopic shear rate $\dot{\gamma}_M$ and apparent viscosity $\eta$ compared to the effective average shear rate $\bar{\dot{\gamma}}$ and viscosity $\bar{\eta}$ of $C_{16}TAB$ in the different segments of the velocity profiles in domain II**

| $\dot{\gamma}_M = 8\ (s^{-1})$ and $\eta = 10$ (mPa·s) | | |
|---|---|---|
| | average values | |
| | $\bar{\dot{\gamma}}\ (s^{-1})$ | $\bar{\eta}$ (mPa·s) |
| segment A | 5.2 | 14 |
| segment B | 10 | 9 |
| $\dot{\gamma}_M = 12\ (s^{-1})$ and $\eta = 14$ (mPa·s) | | |
| | average values | |
| | $\bar{\dot{\gamma}}\ (s^{-1})$ | $\bar{\eta}$ (mPa·s) |
| segment A | 4.4 | 40 |
| segment B | 15.6 | 12 |
| $\dot{\gamma}_M = 20\ (s^{-1})$ and $\eta = 25$ (mPa·s) | | |
| | average values | |
| | $\bar{\dot{\gamma}}\ (s^{-1})$ | $\bar{\eta}$ (mPa·s) |
| segment A | 5.2 | 100 |
| segment B | 22 | 24 |

**Table 5. Macroscopic Shear Rate $\dot{\gamma}_M$ and Apparent Viscosity $\eta$ Compared to the Effective Average Shear Rate $\bar{\dot{\gamma}}$ and Viscosity $\bar{\eta}$ of $C_{14}TAB$ in the Different Segments at $\dot{\gamma}_M = 150\ s^{-1}$ (domain II)**

| $\dot{\gamma}_M = 150\ (s^{-1})$ and $\eta = 5$ (mPa·s) | | |
|---|---|---|
| | average values | |
| | $\bar{\dot{\gamma}}\ (s^{-1})$ | $\bar{\eta}$ (mPa·s) |
| segment A | 76 | 12 |
| segment B | 178 | 6 |
| $\dot{\gamma}_M = 280\ (s^{-1})$ and $\eta = 6$ (mPa·s) | | |
| | average values | |
| | $\bar{\dot{\gamma}}\ (s^{-1})$ | $\bar{\eta}$ (mPa·s) |
| segment A | 245 | 8 |
| segment B | 92 | 21 |

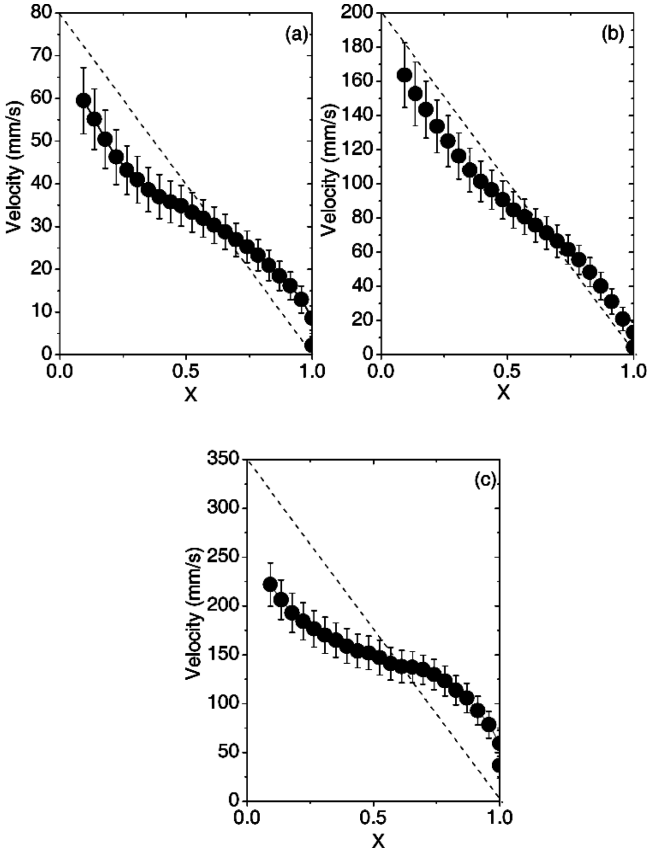


**Figure 8.** Velocity profiles $V(x)$ at high shear rates (domain III) for (a) $C_{18}$TAB at 80 $s^{-1}$, (b) $C_{16}$TAB at 200 $s^{-1}$, and (c) $C_{14}$TAB at 350 $s^{-1}$.

zero at $x = 1$ and the average local viscosity $\overline{\eta} = 7$ mPa·s is close to the viscosity of the system prior to shear-thickening. Therefore, the velocity profile at $\dot{\gamma}_M = 2$ $s^{-1}$ suggests that segment B is constituted of the initial fluid phase (FP) while segment A corresponds to the highly viscous SIS. Moreover, error bars in segment A are significantly larger than those observed in domain I. Such large fluctuations of the local velocity hint to unstable flow in the SIS at the beginning of the transition.

At $\dot{\gamma}_M = 4$ $s^{-1}$, $V(x)$ can no longer be clearly separated into two segments (see Figure 5b). Wall slip reaches nearly 40% of the macroscopic tangential velocity near the moving wall and very strong temporal fluctuations of $V(x)$ are revealed by the large size of the error bars. On average, $V(x)$ decreases roughly linearly with an average value $\overline{\dot{\gamma}} = 1.8$ $s^{-1}$. A possible interpretation of this velocity profile is in terms of a weakly sheared but highly fluctuating SIS that has invaded the whole gap. However, as we shall see below, the three-dimensional features of the flow for $\dot{\gamma}_M \gtrsim 3$ $s^{-1}$ prevent us from drawing definite conclusions.

*2. $C_{16}TAB$ in the Shear-Thickening Domain (II).* Figure 6 shows the flow profiles of $C_{16}$TAB for three different macroscopic shear rates $\dot{\gamma}_M = 8$, 12, and 20 $s^{-1}$. In all cases, two different segments A and B can be roughly distinguished in $V(x)$. Segment A corresponds to a region where the velocity decreases more slowly with $x$ than the corresponding Newtonian profile, leading to an effective local shear rate smaller than the macroscopic one or equivalently to an effective viscosity larger than the macroscopic one (see Table 4). In segment B, $V(x)$ decreases almost linearly with an average shear rate larger than the macroscopic one. While the average viscosity in segment B only changes by a factor of about 3 from $\dot{\gamma}_M = 8$ to 20 $s^{-1}$, $\overline{\eta}$ increases by a factor of almost 100 in segment A. In other words, the average velocity profile gets flatter as the applied shear rate increases in domain II. Moreover, segment A is seen to widen with $\dot{\gamma}_M$ and wall slip at the moving wall is much larger at 20 $s^{-1}$ than for the two smaller shear rates. We interpret these features as the signature of the emergence and growth of a gel-like SIS in segment A. Finally, note that, for the two larger shear rates, error bars are much smaller in segment B than in segment A. We conclude that the flow in segment B is homogeneous and stationary and corresponds to the shear-thinning fluid phase of domain I while the SIS in segment A is subject to strong temporal fluctuations as already reported above for $C_{18}$TAB.

*3. $C_{14}TAB$ in the Shear-Thickening Domain (II).* For $C_{14}$TAB, two shear rates in the shear-thickening domain are shown in Figure 7: $\dot{\gamma}_M = 150$ and 280 $s^{-1}$, with the latter being very close to $\dot{\gamma}_m$. A common feature of the two velocity profiles is the important wall slip at the moving wall. The velocity profile at $\dot{\gamma}_M = 150$ $s^{-1}$ is very similar to that of $C_{16}$TAB at 20 $s^{-1}$, although the effective viscosity is only twice as large in segment A as in segment B (see Table 5). This suggests that the SIS is less viscous in $C_{14}$TAB than in the other two systems. At $\dot{\gamma}_M = 280$ $s^{-1}$, the fluid layer with the smallest apparent viscosity lies close to the rotor (segment A) and supports a local shear rate that is close to the macroscopic one, while the more viscous layer is found close to the stator. This may mean that the SIS has migrated toward the fixed wall. As we shall discuss below, this may also correspond to the flow entering a three-dimensional unstable but still rather stationary state.

**C. Velocity Profiles at High Shear Rates (Domain III).** In this last shear rate domain, the three micellar systems are shear-thinning and the viscosity curves superimpose whatever the length of the aliphatic chain (see Figure 2). In a previous paper dealing with SANS experiments under flow,[10] we showed that the scattered intensity distributions are also qualitatively the same for the three systems: highly anisotropic patterns are collected that result from a high degree of orientation of the micelles along the flow direction. As a consequence, the three solutions are rheologically equivalent and it should not be surprising that the velocity profiles are qualitatively the same. Indeed, as seen in Figure 8 for each surfactant at a shear rate representative of domain III, all the velocity profiles have similar shapes although the amount of apparent wall slip at the rotor varies from one system to another.

Here the flow cannot be clearly divided into different layers with well-defined effective viscosities, and the local shear rate rather varies continuously through the gap leading to S-shaped profiles. The simplest interpretation of such smooth velocity profiles is in terms of a radial component that adds up to the contribution of the tangential velocity in the USV measurement (see eq 1).[23] More precisely, the velocity profiles of Figure 8 are typical of those obtained in flows involving Taylor-like vortices.[26−28] Indeed, in a simple three-dimensional flow constituted of stationary toroidal vortices, the radial component brings either a positive or a negative contribution to the tangential velocity depending on the radial position and on the vortex location, resulting in an S-shaped $V(x)$. This indirect picture will be confirmed below through direct flow visualization.

**D. Wall Slip Magnitude.** As seen above, the velocity inside the sample and close to the moving wall is most often much smaller than the tangential velocity $V_M$ of the rotor. This apparent

(26) Kikura, H.; Takeda, Y.; Durst, F. *Exp. Fluids* **1999**, *26*, 208.
(27) Takeda, Y. *J. Fluid Mech.* **1999**, *389*, 81.
(28) Akonur, A.; Lueptow, R. M. *Phys. Fluids* **2003**, *15*, 947.

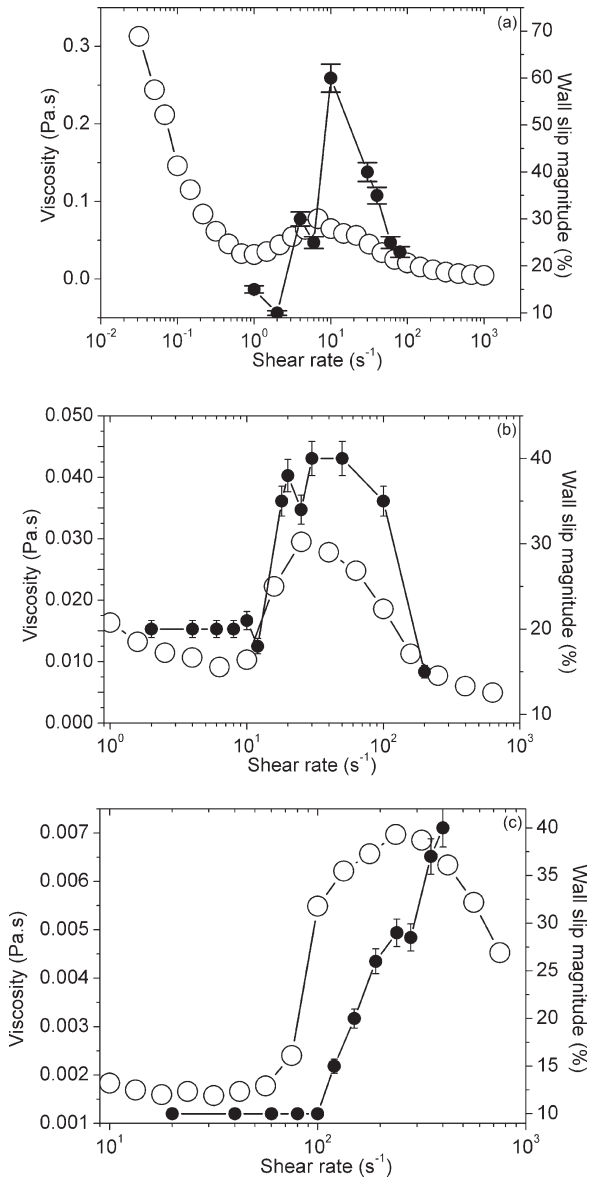


**Figure 9.** Wall slip amplitude $W_s$ at the rotor (●) and apparent viscosity $\eta$ (○) as a function of the macroscopic shear rate for (a) $C_{18}$TAB, (b) $C_{16}$TAB, and (c) $C_{14}$TAB.

wall slip is usually attributed to the presence of a lubrication layer whose width is smaller than the USV spatial resolution of 40 $\mu$m. Significant apparent slip velocities may also be recorded at the stator, but in general these remain small compared to those at the rotor. Such wall slip phenomena have already been reported in previous studies on micellar systems,[22,24,29] but since they appear as a central feature of the present results, we shall describe them more quantitatively by focusing on the wall slip magnitude $W_s$ defined as

$$W_s = \frac{V_M - V_F}{V_M} \quad (5)$$

where $V_F$ stands for the fluid velocity close to the rotor, which is estimated experimentally by linear extrapolation of $V(x)$ to $x = 0$ over about 150 $\mu$m close to the rotor.

Figure 9 shows that $W_s$ strongly depends on the macroscopic shear rate supported by the sample and reaches a maximum of about 60% for $C_{18}$TAB which also has the highest apparent viscosity in the shear-thickening domain. When plotting the apparent viscosity $\eta$ together with $W_s$ versus the shear rate for the three systems, it turns out that the wall slip amplitude is strikingly correlated to $\eta$.

In domain I, for $C_{16}$TAB and $C_{14}$TAB, the slip magnitude $W_s$ remains roughly constant and equal, respectively, to 20% and 10%, while $\eta$ only slightly decreases (see Figure 9b and c). For $C_{18}$TAB, we have only been able to measure one velocity profile in domain I (for $\dot{\gamma} = 1\ s^{-1}$) and $W_s$ is about 15% (see Figure 9a).

When the macroscopic shear rate reaches the critical value $\dot{\gamma}_c$, $W_s$ increases sharply with the shear rate. For $C_{18}$TAB and $C_{16}$TAB, a maximum is observed in $W_s$ that roughly corresponds to the maximum in apparent viscosity in the shear-thickening transition. Beyond the viscosity maximum, $W_s$ is seen to decrease in domain III. For $C_{14}$TAB, however, wall slip increases continuously throughout domains II and III. The maximum wall slip magnitudes measured near the rotor are approximately 60, 45, and 40% for $C_{18}$TAB, $C_{16}$TAB, and $C_{14}$TAB, respectively.

## V. Summary and Discussion

In summary, the velocity profiles recorded in three low-concentration micellar systems made of $C_{18}$TAB, $C_{16}$TAB, and $C_{14}$TAB reveal similar features throughout the shear-thickening transition. Below $\dot{\gamma}_c$, the flow is homogeneous with a small amount of wall slip. At the onset of the shear-thickening regime, a weakly sheared layer is observed close to the rotor that we attribute to the emergence and growth of a gel-like SIS. The fluid layer close to the fixed wall has an effective viscosity of the same order of that of the system prior to shear-thickening and is interpreted as the initial fluid phase (FP). Shear-thickening coincides with a strong increase of apparent wall slip at the rotor (up to 60% of the imposed wall velocity). This is consistent with a gel-like SIS that slides against the wall through a thin lubrication layer, while the FP at the stator shows much smaller wall slip.

Previous birefringence and SANS experiments[5,10] suggest that the SIS average orientation is close to the flow direction. Here, the observation of a very viscous SIS confirms older experiments on other dilute CTAB/NaSal and TTAA/NaSal systems[8,15,30,29] and provides more quantitative insights. Furthermore, the present study allows us to directly compare the behavior of three different surfactants and to question the influence of the aliphatic chain length. In particular, the SIS seems much more viscous and subject to larger temporal fluctuations in $C_{18}$TAB (see Figure 5a). In $C_{16}$TAB and $C_{14}$TAB, no true pluglike flow is observed in the SIS which rather supports a finite shear rate that gets larger as the chain length is decreased (compare Figures 6b and 7a). Except maybe for $C_{18}$TAB at the end of domain II (see Figure 5b) and at the very beginning of domain III (data not shown), our measurements do not show total wall slip and solid-body rotation of a SIS that fills the whole gap of the Couette device as reported in ref 29 on a 1.7 mM equimolar TTAA/NaSal solution. Instead, the above heterogeneous flow, characterized by two layers in the radial direction, gives way to a more complex picture with large temporal fluctuatuations in the SIS and S-shaped velocity profiles in domain III that hint to three-dimensional unstable flows.

Direct visual inspection in a transparent device shows that the flow is also not homogeneous along the vertical direction for the three solutions at the end of domain II and in domain III. Figure 10 shows pictures of the $C_{18}$TAB sample taken in the vorticity-tangential velocity plane ($\vec{\omega}$, $\vec{V}$) at $\dot{\gamma}_M = 3$ and 8 $s^{-1}$. These

(29) Hu, Y. T.; Boltenhagen, P.; Matthys, E.; Pine, D. J. *J. Rheol.* **1998**, *42*, 1209.
(30) Hu, Y. T.; Boltenhagen, P.; Pine, D. J. *J. Rheol.* **1998**, *42*, 1185.

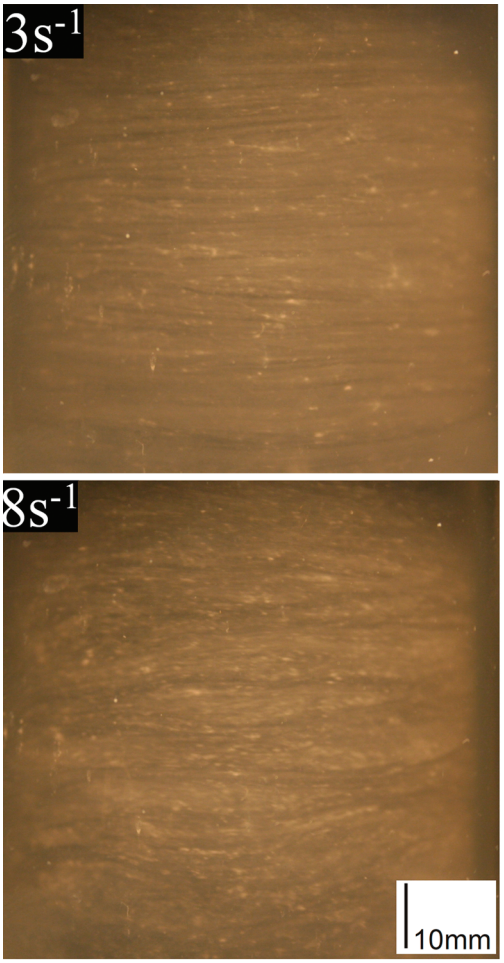


**Figure 10.** Flow visualizations in the vorticity−velocity gradient plane ($\omega$, $\vec{\nabla}V$) of $C_{18}$TAB/NaSal at 3 mM/3 mM in the shear-thickening domain for $\dot{\gamma}_M = 3$ (top) and 8 $s^{-1}$ (bottom). The bar gives the scale of the picture.

visualization experiments were conducted in a Plexiglas Couette device with $R_1 = 23.5$ mm, $R_2 = 25$ mm, and $H = 70$ mm. At $\dot{\gamma}_M = 3\ s^{-1}$, a vertical stratification is observed with alternately off-white and darker macroscopic domains of thickness of about 1 mm. This is strongly reminiscent of previous observations on similar surfactant systems.[15,30] Such a structure of bands stacked in the vorticity direction provides strong support for a three-dimensional unstable flow constituted of Taylor-like vortices. When the shear rate is increased to $\dot{\gamma}_M = 8\ s^{-1}$, the apparent order is broken and the vorticity bands become strongly distorted and fluctuating. Similar obervations were made on the other two surfactant solutions containing small polystyrene particles although pictures taken with the $C_{16}$TAB and $C_{14}$TAB samples suffered from a lack of contrast. Therefore, in all cases, a flow instability most likely occurs in the SIS (see also the large error bars in Figures 5 and 6) leading to three-dimensional flow.

In the above visualizations, it is not clear whether the optical contrast arises from the micellar aggregates themselves or from the migration of the seeding particles into a roll-like structure. More experiments, such as scans of the velocity profiles along the vertical direction, would be necessary to draw definite conclusions. Still, a number of clues indicate the presence of three-dimensional flows. We believe that these flows result from an elastic instability of the gel-like SIS. Indeed, such a mechanism has been invoked to explain vorticity banding in some shear-thickening rodlike colloidal suspensions (see ref 31 and references therein). It is also now clearly established that some shear-thinning semidilute micellar systems present an instability in the shear-banding regime.[32] This instability is characterized by the presence of Taylor-like vortices[33] and is compatible with an elastic instability in the highly aligned viscoelastic SIS.[34−36] Another possible interpretation could lie in an intrinsic instability of the interface driven by a jump in second normal stress across it,[36,37] but in the case of a gel-like SIS we believe a bulk elastic instability to be more likely.

## VI. Conclusion and Open Questions

In this experimental study, we have presented macroscopic rheological data as well as local velocity profiles of dilute shear-thickening micellar solutions. The shear-induced properties involved in the local flow behavior were described for the various surfactant chain lengths.

The addition of small polystyrene particles only slightly modifies the rheological behavior of the dilute micellar systems and does not affect the shear-thickening phenomenon. At low shear rates, the velocity profiles are very similar to those of a Newtonian fluid, that is, a single homogeneous layer. In the shear-thickening domain, the flow becomes inhomogeneous and velocity profiles show the coexistence of two structurally different phases: the shear induced structure (SIS) mixed to the initial fluid phase. In some velocity profiles, the nearly flat central segment indicates that the SIS offers a strong resistance to the flow. This suggests that the micelles somehow merge to form a gel-like SIS that slips at the moving wall. Together with local velocity measurements, direct observations in the vorticity−velocity plane allowed us to conclude that the flow of shear-thickening micellar solutions eventually becomes three-dimensional.

Still, the present results raise many open questions that should be addressed in subsequent work. For instance, the exact microscopic nature of the SIS remains unknown and structural characterization under shear is greatly needed to choose between the various models of shear-thickening available in the literature. Experimental measurements, such as two-dimensional flow mapping, would allow one to discriminate between the various instability mechanisms and to better characterize the three-dimensional unstable flows that were revealed here. Finally, the question of whether or not the features observed in the present experiments are general and characteristic of shear-thickening systems should also be investigated through more measurements on other micellar and colloidal systems.

(31) Dhont, J. K. G.; Briels, W. J. *Rheol. Acta* **2008**, *47*, 257.
(32) Lerouge, S.; Argentina, M.; Decruppe, J. P. *Phys. Rev. Lett.* **2006**, *96*, 088301.
(33) Fardin, M. A.; Lasne, B.; Cardoso, O.; Grégoire, G.; Argentina, M.; Decruppe, J.-P.; Lerouge, S. *Phys. Rev. Lett.* **2009**, *103*, 028302.
(34) Lerouge, S.; Fardin, M.-A.; Argentina, M.; Grégoire, G.; Cardoso, O. *Soft Matter* **2008**, *4*, 1808.
(35) Fardin, M. A.; Lasne, B.; Cardoso, O.; Grégoire, G.; Argentina, M.; Decruppe, J.-P.; Lerouge, S. the XVth international congress of rheology, Monterey (5-8 August 2008).
(36) Fielding, S. M. *Phys. Rev. Lett.* **2010**, *104*, 198303.
(37) Fielding, S. M. *Phys. Rev. E* **2007**, *76*, 016311.